Supporting Online Material for

Experimental Observations of Stress-Driven Grain Boundary Migration

T. J. Rupert, D. S. Gianola, Y. Gan, K. J. Hemker*

*To whom correspondence should be addressed. E-mail: hemker@jhu.edu

Published 18 December 2009, *Science* **326**, 1686 (2009)
DOI: 10.1126/science.1178226

This PDF file includes:

Supporting Online Material for
Experimental Observations of Stress-driven Grain Boundary Migration

T.J. Rupert[1,2], D.S. Gianola[1,3], Y. Gan[4], K.J. Hemker[1,†]

[1] Department of Mechanical Engineering, Johns Hopkins University, Baltimore, MD, USA

[2] Department of Materials Science & Engineering, Massachusetts Institute of Technology, Cambridge, MA, USA

[3] Department of Materials Science and Engineering, University of Pennsylvania Philadelphia, PA, USA

[4] Institute for Materials Research II, Karlsruhe Institute of Technology, Karlsruhe, Germany

[†] Email: hemker@jhu.edu

Materials and Methods

Material synthesis and specimen fabrication

Standard Si-based microfabrication techniques were used to make thin film tensile specimens. Photolithography was utilized in conjunction with a number of etching techniques (KOH wet etching, deep reactive ion etching, and pulsed XeF_2) to define features on a {100} silicon wafer. Backside wafer processing was used to produce silicon frames (1 cm x 1 cm), which provided a base for film deposition and served as sample grips for the handling and deformation of the films. Frontside micromachining was used to define the tensile geometries

detailed in the body of this paper. The gage widths and lengths of the specimens were 700 μm and 4 mm, respectively. Details of this microfabrication process are provided in [S1].

The thin film specimens were deposited using electron beam evaporation of 99.999% pure Al. Deposition was initiated when the chamber pressure reached 1 x 10^{-7} Torr to ensure a low level of impurities in the films. The films for this study were deposited at a rate of 4 Å/s (at ambient temperature) to encourage a fine microstructure. A pulsed technique was utilized where deposition was interrupted every ~20 nm and the source material was allowed to cool. This pulsed technique helped to ensure that a columnar grain structure did not develop in the films. The films studied here had thicknesses of 150-220 nm with average grain sizes of 60-90 nm.

Microspecimen tensile testing

The basic layout of the tensile testing setup consisted of one fixed grip connected to a load train and another grip which could be moved either by a piezoelectric screw-driven linear picomotor (for tensile elongation) or a 5-axis motorized stage (for sample alignment). The 5-axis stage was used in unison with a stereoscopic microscope to precisely align the grips with each other. Next, the silicon sample frame was placed on top of the grips and aligned using the edge of the silicon die as a guide. A combination of UV-curing glue and Loctite 414 was used to adhere the specimen to the grips. The Si support strips were then cut using a Dremel rotary tool with a diamond-impregnated blade attached to a 3-axis stage. The rotary blade was carefully brought into contact with the strip and slowly advanced through the strip to prevent large vibrations or rotation of the die from damaging the thin film. The freestanding films were then pulled in tension using the picomotor. A nominal strain rate of 5 x 10^{-5} s^{-1} was used for all tensile tests performed for this study.

TEM grain size measurements

Once the desired displacements were reached, the films were unloaded, then cut from the Si frame by carefully running a scalpel along the inside edge of the grip. The free film was subsequently mounted onto a copper TEM grid after lightly coating with adhesive. Specimens were observed in a Philips EM 420 operated at 120 kV, predominantly in bright field mode. The film studied here are electron transparent as-deposited, removing the possibility of artifacts from sample preparation influencing characterization results. The imaged microstructures were analyzed using computer software to provide a complete description of each grain in terms of parameters such as area, aspect ratio, major and minor axis length, etc.

Specimens were moved to specific locations around the added stress concentrations at low-magnification. After zooming in, bright-field images were taken from an area of approximately 5 μm by 5 μm centered at the locations of interest. The size of each grain was determined by finding a circle equivalent diameter from the measured grain area. Over 100 grains were measured from each region of interest to fully characterize the microstructure. Grain size distributions are presented as area-weighted cumulative distributions functions to avoid errors which can arise when presenting distributions as histograms with arbitrary bin sizes. The use of cumulative distribution functions also facilitates easy comparison of different regions.

Finite element simulations

The full-field spatial distributions of stress and strain were computed for the various specimen geometries using a commercial finite element modeling package (ABAQUS). The geometry, taken from the experimental setup, has been meshed by hybrid triangle and quadrilateral shell elements. The shell elements were implemented in ABAQUS as general-

purpose conventional shell elements (S4R and S3R) with a large-strain formulation, allowing transverse shear deformation. These types of element are valid also for thick shell element.

The size of the shell elements is approximately 10 times larger than the film thickness but smaller than the typical expected wavelength of the wrinkling pattern as observed in experiments. The mesh was refined in regions containing rapidly changing stresses, e.g. near the holes and wrinkled regions.

The simulations employed an elasto-plastic constitutive law using a von Mises yield criterion and isotropic hardening, which was based on experimental stress strain curves from tensile testing of a specimen without patterned holes in the gage section [S1]. In order to separate the contributions of different stress states on grain growth in our nanocrystalline thin films, we analyzed the simulations in terms of the work done by distortional energy and volumetric energy, which can be related to shear and normal stresses, respectively. The simulation output was analyzed as follows. For a quasi-static deformation, the total strain energy is the summation of the elastic strain energy $\boldsymbol{W^e}$, and plastic dissipation energy $\boldsymbol{W^p}$. For an isotropic material (we assume Al to be isotropic since the anisotropy ratio of the elastic constants, given by $A = (C_{11} - C_{12})/2 - C_{44}$, where A=1 for a perfectly isotropic material, is only 1.2), the elastic strain energy can be separated into the distortional and volumetric parts as:

$$W^e = \frac{1+\nu}{3E}\sigma_{eq}^2 + \frac{3(1-2\nu)}{2E}\sigma_m^2 \ .$$

Here, σ_{eq} is the von Mises stress, σ_m the hydrostatic pressure, and E and ν the Young's modulus and Poisson's ratio, respectively. According to the von Mises yield criterion, the plastic dissipation energy is the work done by the deviatoric stress alone. Thus, we can write the total distortional energy and volumetric energy as:

$$W^{dist} = \frac{1+\nu}{3E}\sigma_{eq}^2 + W^p \quad ,$$

$$W^{vol} = \frac{3(1-2\nu)}{2E}\sigma_m^2 .$$

We performed instability calculations using finite element modeling to understand the complex deformation state that arises in the thin film geometry. Thin stressed membranes are known to develop instabilities that cause the material to wrinkle out-of-plane, and when properly modeled, this phenomenon can be exploited as a sensitive mechanical assay for strain in thin materials. Some examples include stretching of thin elastic sheets [S2, S3], wrinkling of stretched skin and biological cells [S3], and axisymmetric wrinkling of polymer sheets by surface tension-induced capillary forces from water droplets [S4]. The complex stress states generated in films with intentional defects (stress concentration holes) caused periodic wrinkling in all films studied here. Analytical solutions for wrinkling caused by the stress states induced in these films are not tractable, although numerical solutions are possible and were obtained using finite element modeling. All finite element modeling results presented here include the effects of out-of-plane displacements during the course of deformation. Experimental wrinkling patterns, where the peaks and troughs of individual wrinkles are highlighted by light reflecting from mirror-like surfaces, were compared with those obtained by finite element modeling to validate all subsequent stress and strain analyses. We compared quantities such as the density, wavelength, and persistence length (defined as the length of a wrinkle before transitioning to a taught region of the film) of the experimental wrinkling pattern to the simulations.

Post-buckling analyses were performed based on the arc length method (known as the RIKS method [S5, S6]). Due to the nonlinearity in geometry and plastic behavior, an appropriate

maximum arc length was chosen by trial and error to achieve convergence of the problem (0.1%~0.2% of the total loading time). We also studied configurations with and without pre-stressed state. The pre-stress state was introduced by a virtual increase of film temperature, and as a result, a biaxial compression state was imposed on the film. The magnitude of this biaxial stress was estimated in the range between 10 to 50 MPa, which is similar to reported values given from in situ growth experiments of low melting temperature material thin films after accounting for stresses from the thermal expansion mismatch between Al and Si [S7]. During the release process of this biaxial compressive stress, an initial wrinkling pattern can be represented in simulation. Finally, the edges of the film were stretched to approximately 25-30 μm to mimic the performed experiments. A representative image of the computed wrinkling pattern as compared to an experimental image with the same imposed displacement and lighting conditions is shown in Figure S1.

Supplemental Tables and Figures

Table S1: Summary of experiments performed to determine effect of deformation on grain growth in nanocrystalline Al thin films. The top section tabulates quantities that separate the effect of stress and strain, while the bottom data show the difference between stress state as given by volumetric (normal stresses) and distortional (shear stresses) energy density values. The specimen names represent the geometry of the patterned holes, which introduce spatial variations in stress and strain during deformation.

Stress vs. Strain							
Specimen	*Region*	*1st Principal Stress (MPa)*	*Max Shear Stress (MPa)*	*1st Principal Strain*	*Plastic Equivalent Strain*	*Grain Size (nm)*	*% change from AD*
Horizontal	AD					81 ± 27	
	Near Edge	187	187	0.032	0.029	124 ± 47	53
	Above	190	190	0.012	0.010	134 ± 50	65
Angled 1	AD					93 ± 29	
	Near Edge	240	240	0.27	0.27	140 ± 58	51
	Above	258	257	0.15	0.16	176 ± 65	89
Stress State (Normal vs. Shear)							
Specimen	*Region*	*Volumetric Energy Density (J/m^3)*	*Distortional Energy Density (J/m^3)*			*Grain Size (nm)*	*% change from AD*
Angled 2	AD					61 ± 24	
	Above Inner	3.30×10^4	5.9×10^5			110 ± 47	80
	Above	1.0×10^4	1.2×10^6			136 ± 64	123
	Above Outer	1.1×10^4	2.4×10^5			103 ± 39	69
Angled 3	AD					93 ± 29	
	Above Inner	2.9×10^4	4.5×10^5			142 ± 52	53
	Above	1.2×10^4	1.2×10^6			176 ± 65	89
	Above Outer	1.2×10^4	2.4×10^5			122 ± 46	31

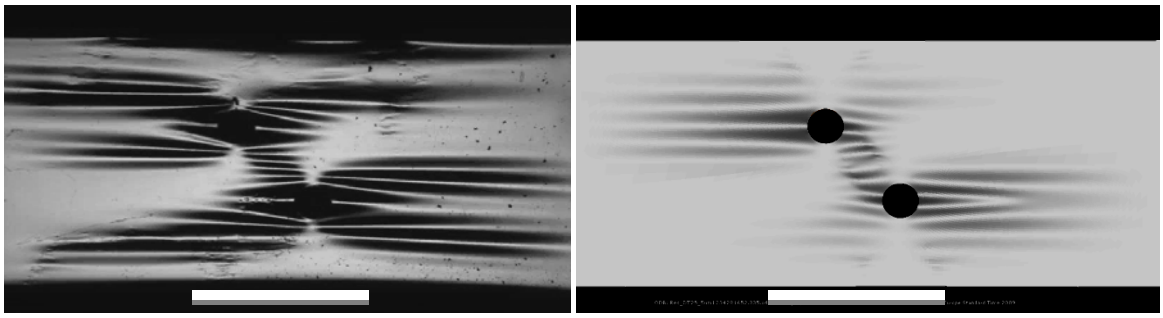

Figure S1: Experimentally observed (left) and simulated (right) wrinkling patterns during tensile testing of a 2 hole Al thin film. The imposed remote axial displacement is 20 μm. The lighting is normal to the surface of the unwrinkled film in both cases. The scale bars represent 500 μm.

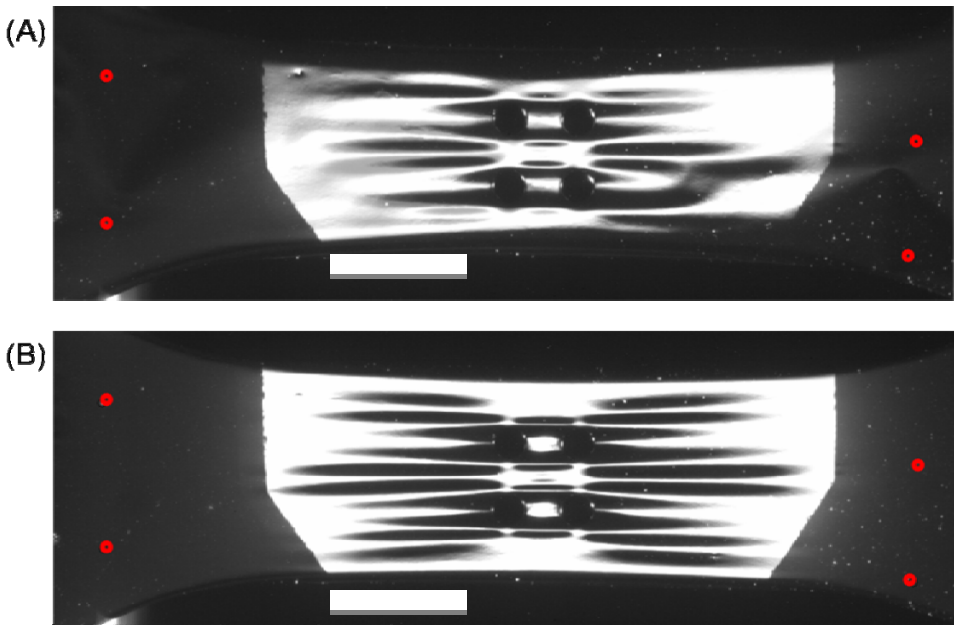

Figure S2: Images of a 4-hole specimen with the motion of four peaks (marked by red circles) being calculated by digital image tracking. (A) Specimen before being pulled taut. (B) Specimen after ~15 μm displacement has been applied. The scale bars represent 500 μm.

Table S2: Comparison of displacement values measured by capacitance gage and image-based techniques.

Specimen Type	Capacitance Displacement (μm)	Image-Based Displacement (μm)	Difference (μm)	% Difference
Horizontal	30	29.1	0.9	3.1
Angled	25	23.7	1.3	5.5
4-hole	25	24.3	0.7	2.9

Supplemental References

[S1] D. S. Gianola *et al., Acta Mater.* **54**, 2253 (2006).

[S2] E. Cerda, K. Ravi-Chandar, L. Mahadevan, *Nature* **419**, 579 (2002).

[S3] E. Cerda, L. Mahadevan, *Phys. Rev. Lett.* **90**, 074302-1 (2003).

[S4] J. Huang *et al., Science* **317**, 650 (2007).

[S5] E. Riks, *J. Appl. Mech.* **39**, 1060 (1972).

[S6] E. Riks, *Int. J. Solids Struct.* **15**, 529 (1979).

[S7] J.A. Floro *et al., J. Appl. Phys.* **89**, 4886 (2001).